Contact dynamics on net capturing of tumbling space debris

Shan, Minghe; Guo, Jian; Gill, Eberhard

DOI
10.2514/1.G003460

Publication date
2018

Document Version
Accepted author manuscript

Published in
Journal of Guidance, Control, and Dynamics

Contact Dynamics on Net Capturing of Tumbling Space Debris

Minghe Shan[a], Jian Guo[b] and Eberhard Gill[c]
Delft University of Technology, Delft, 2629 HS, the Netherlands

I. Introduction

Operational space missions are more and more endangered by millions of space debris objects [1]. To mitigate this risk, many space debris capturing and removal methods have been proposed [2], such as the robotic arm removal method [3, 4], the tethered space robot [5, 6], and the harpoon system [7]. Among these methods, the net capturing concept is considered as one of the most promising capturing methods due to multiple advantages: it allows a large distance between the chaser satellite and the target, such that close rendezvous and docking is not mandatory; it is compatible with various dimensions and shapes of space debris objects, especially with those of large space debris objects; and, finally, the net is flexible, lightweight and cost efficient.

Currently, net capturing for space debris removal is an international research focus. Several projects under this concept have been funded by European Space Agency (ESA) and simulations on the net capturing have been extensively performed [8, 9]. Yang et al. have investigated the rotating and non-rotating net deployment dynamics, along with the analysis on the impact simulation and the net-closing simulation [10]. Botta et al. have analyzed the effect of bending stiffness of cables on the deployment dynamics [11], and investigated contact dynamics during capturing by applying a continuous compliant approach for the normal contact force and a modified damped bristle model for the friction force [12]. A necessity of a closing mechanism has been discussed by Sharf et al. [13]. Besides, several other simulators of net deployment and net capturing for space debris have been developed. Benvenuto et al. have developed a simulator based on a mass-spring model and explored

[a] PhD candidate. Faculty of Aerospace Engineering, m.shan@tudelft.nl
[b] Assistant professor. Faculty of Aerospace Engineering, j.guo@tudelft.nl
[c] Full professor. Faculty of Aerospace Engineering, e.k.a.gill@tudelft.nl

the net capturing based on the penalty-based method [14, 15]. In contrast, Gołębiowski et al. have developed a simulator based on Cosserat rod theory and simulated the net contacting with a target using the predictor-corrector algorithm [16]. Shan et al. have developed a simulator for net deployment based on a mass-spring model and an absolute nodal coordinate formation [17]. Benvenuto's, Gołębiowski's and Shan's net simulators have been validated by parabolic flight experiments [18–20]. Gołębiowski's and Shan's validations used the dataset from the same experiment.

However, the acceptable tumbling rate of space debris captured by a net is still not well understood in spite of the extensively existing research. The present paper provides several contributions to the already existing body of knowledge. First, a contact dynamics modeling method, named impulse-based method, is applied to the tumbling space debris capturing scenario for the first time. A comparison is made between the simulation and the parabolic flight experiment of a fixed Envisat mockup capturing. The model is therefore validated and its effectiveness is demonstrated. Second, the tumbling target capturing without a closing mechanism is investigated. If viable, this will deduce the complexity of the capturing vehicle. The range of tumbling rates without a closing mechanism are provided and the stability of the system is discussed. Finally, a closing mechanism is designed and integrated to the net capturing system to ensure a successful capturing of a target, especially that with a higher tumbling rate, to reduce the risk of slipping out of the net. Its ability to do so is studied in simulation.

II. Dynamics of the Net Capturing System

A. Dynamics of a Net

A mass-spring model is the basis for simulation of net dynamics. A mass-spring model approximates a flexible cable as a series of mass points connected by mass-less spring-damper elements. The geometrical and physical configuration of the net is shown in Fig. 1. Four bullets are attached at the corners of the net with additional cables. The mass points of the net are numbered sequently as a matrix as shown in Fig. 1. According to the nature of the cable material, a cable cannot be compressed, and a tension force will only be generated when the cables are fully extended. The model of the tension force and the dynamic equations of motion for the entire net have been established by Shan et al. [17].

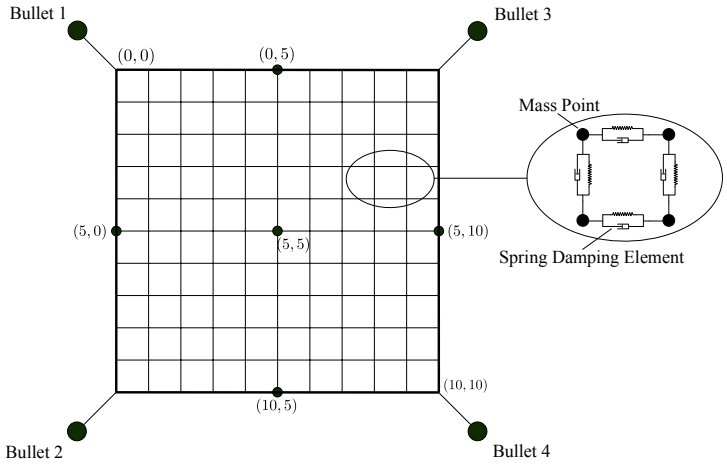

Fig. 1 Geometrical and physical configuration of a net.

B. Dynamics of a Tumbling Target

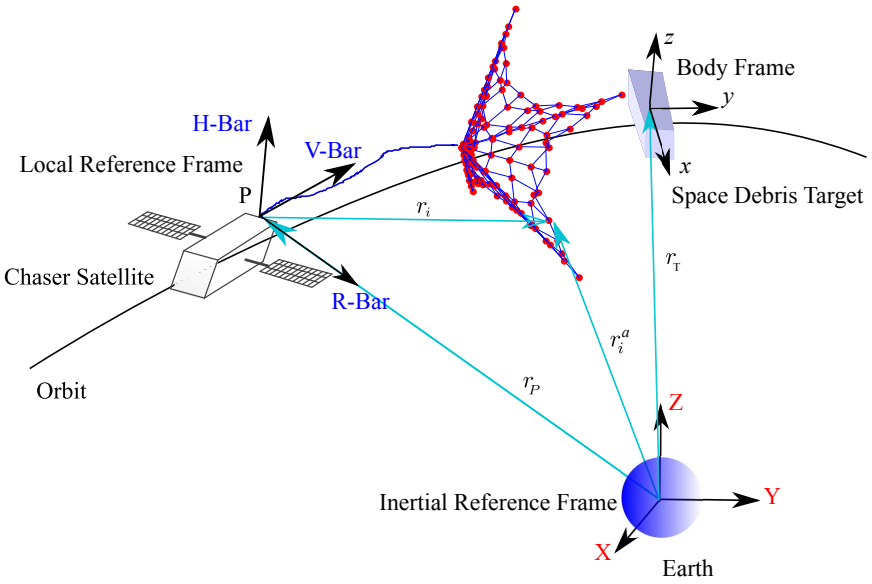

Fig. 2 Target approached by chaser satellite along V-Bar.

The chaser satellite is assumed to be approached along track with the target before shooting the net (Fig. 2). The non-cooperative target introduced in this paper has an initial tumbling rate along its minimum or maximum inertia axis. The contact with the net might change the motion of the target. Therefore, a contact force is included in the translational and rotational dynamics of

the target, which is expressed as

$$m_T \ddot{\boldsymbol{r}}_T = \boldsymbol{f}_C + \boldsymbol{f}_E + \boldsymbol{g}_T,$$
$$\boldsymbol{I}\dot{\boldsymbol{\omega}}_{\boldsymbol{T}} + \boldsymbol{\omega}_{\boldsymbol{T}} \times \boldsymbol{I}\boldsymbol{\omega}_T = \boldsymbol{t}_C + \boldsymbol{t}_E, \tag{1}$$

where, m_T and $\boldsymbol{I}$ is the mass and the inertia of the target, respectively; $\boldsymbol{r}_T$ represents the position vector of the center of mass of the target in the inertial frame; $\boldsymbol{\omega}_T$ is the angular velocity of the target in the target body frame (see Fig. 2). Here, $\boldsymbol{f}_C$, $\boldsymbol{f}_E$, and $\boldsymbol{g}_T$ is the contact force, external force (including disturbances) and the gravitational force acting on the target, respectively. In addition, $\boldsymbol{t}_C$ and $\boldsymbol{t}_E$ represent the contact torque and the external torque acting on the target, respectively.

III. Contact Dynamics of Net Capturing

The algorithm of capturing a target using a net is shown in Fig. 3. Contact detection needs to be performed at every step of simulation, and contact dynamics takes over when a contact, either a single contact or multiple contacts, is detected. This section presents the contact detection algorithm and the modeling of contact dynamics.

A. Contact Detection

In this paper, the contact detection, based on the Axis-Aligned Bounding Box (AABB) method [21], is divided into two levels (Fig. 4) so as to improve the computational performance of the simulation. The bounding box is the box with the smallest measure (volume in this paper) within which all the points on the target lie. In the first level of detection, the net and the target are assumed to be contained in the box N and the box T, respectively. Therefore, the contact detection is only performed between these two boxes. The second level of contact detection starts once the two boxes intersect with each other. In the second level of detection, every node of the net is checked by calculating the minimum distance d between the node and the target. Once the distance d is smaller than a threshold distance ϵ, a respective contact response will be applied on the node. The contact response depends on the number and position of the contacting points.

B. Impulse-Based Method

The impulse-based method is commonly used in game and virtual reality environments, especially the contact between two separate bodies [22]. This paper applies this method to the contact

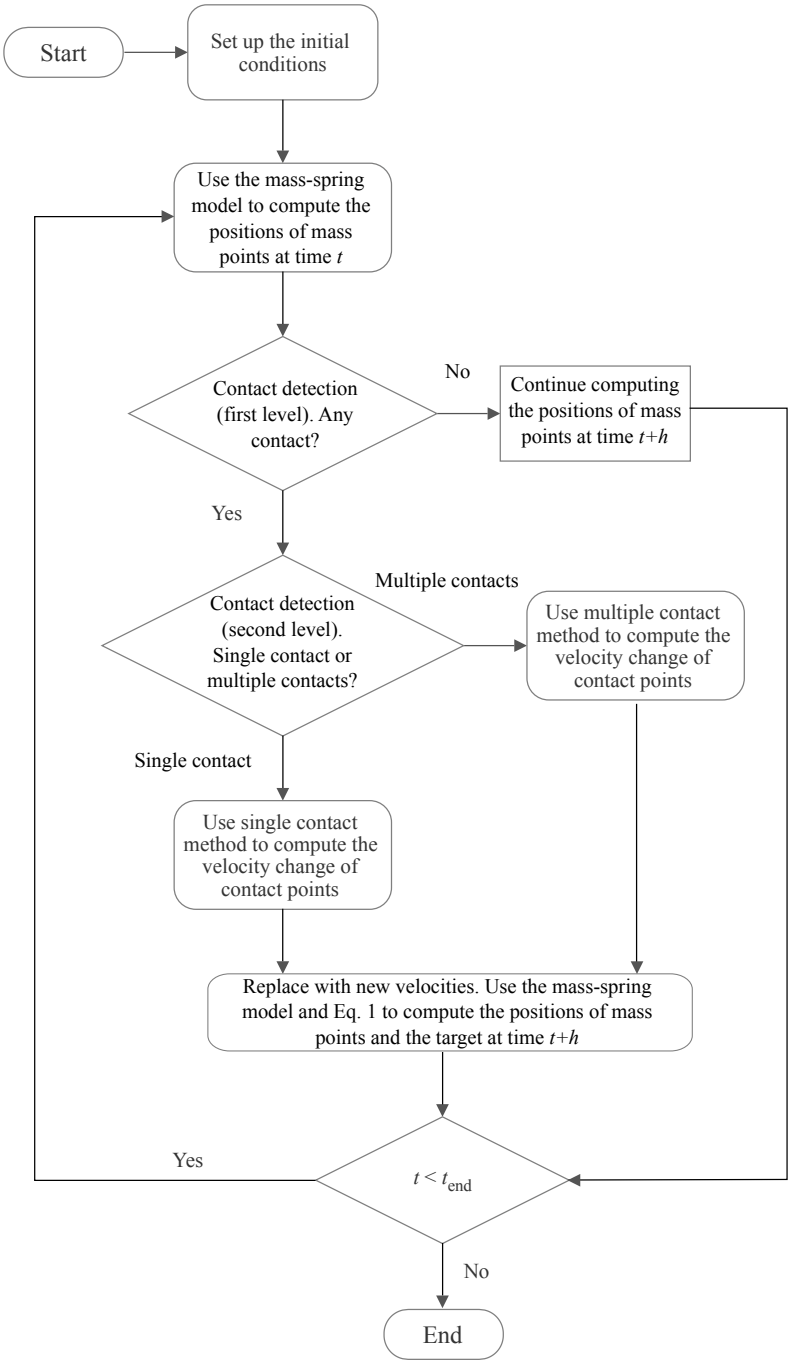

Fig. 3 Flowchart of the impulse-based method on space debris capturing.

dynamics of a tumbling space debris removal using a net. As introduced previously, the net can be discretized into mass points connected under a specific configuration. Therefore, a net contacting with a target can be considered as a single mass point or multiple mass points contact with one single object. The number of contacting mass points depends on the relative position of the net and the target.

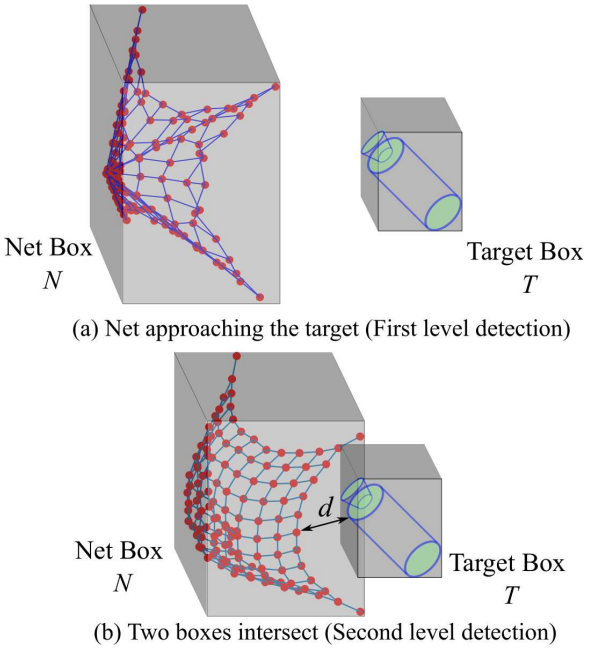

Fig. 4 Contact detection.

1. Single Contact on One Target

In the impulse-based method, the impulse instead of the contact force caused by the contact, is calculated. Therefore, the velocity change after contact can be computed. The coefficient of restitution is defined from the relative velocity change as

$$e = -\frac{v_r^+}{v_r^-}, \tag{2}$$

where $0 \leq e \leq 1$. In this paper, superscript '-' and '+' indicate the status before and after the contact. Thus, v_r^+ is the relative velocity of two objects in the direction normal to the plane of contact after contact, and v_r^- is the relative velocity of two objects in the direction normal to the plane of contact before contact. When $e = 0$, then $v_r^+ = 0$, the contact is fully inelastic, and when $e = 1$, $v_r^+ = -v_r^-$, the contact is fully elastic. In this paper, since the mass of the target is much larger than the net, we assume the contact between the net and the target is fully elastic and $e = 1$ in the simulation. Assume a single mass point P contact with a tumbling object O whose angular velocity is $\boldsymbol{\omega}_O$. The position of the mass point is $\boldsymbol{r}_P$, and the position of the center of mass of the object is $\boldsymbol{r}_O$. Velocities of P and O are $\boldsymbol{v}_P$ and $\boldsymbol{v}_O$, respectively. Let $\boldsymbol{n}$ represent the normal direction of the contact plane on object O. Velocities and angular velocities after contact can then

be expressed as

$$\begin{aligned} \boldsymbol{v}_P^+ &= \boldsymbol{v}_P^- + j\boldsymbol{n}/m_P, \\ \boldsymbol{v}_O^+ &= \boldsymbol{v}_O^- - j\boldsymbol{n}/m_O, \\ \boldsymbol{\omega}_O^+ &= \boldsymbol{\omega}_O^- - \boldsymbol{I}_O^{-1}(\boldsymbol{r}_{OC} \times j\boldsymbol{n}) \end{aligned} \tag{3}$$

where m_P and m_O are masses of two contact objects, j is the impulse generated from the contact, and $\boldsymbol{r}_{OC} = \boldsymbol{r}_C - \boldsymbol{r}_O$ is the relative position of the contact point C with respect to the center of mass of object O. Therefore, the relative velocity along the direction normal to the contact plane can be expressed as

$$\begin{aligned} v_r^+ &= \boldsymbol{n}(\dot{\boldsymbol{r}}_P^+ - \dot{\boldsymbol{r}}_{OC}^+), \\ v_r^+ &= \boldsymbol{n}(\boldsymbol{v}_P^+ - (\boldsymbol{v}_O^+ + \boldsymbol{\omega}_O^+ \times \boldsymbol{r}_{OC})) \end{aligned} \tag{4}$$

Substituting Eq. 3 into Eq. 4, yields

$$j = \frac{-(e+1)v_r^-}{1/m_P + 1/m_O + \boldsymbol{n}((\boldsymbol{I}_O^{-1}(\boldsymbol{r}_{OC} \times \boldsymbol{n})) \times \boldsymbol{r}_{OC})}. \tag{5}$$

The velocities of two objects after contact can be achieved by the computed impulse j using Eq. 3.

2. *Multiple Contacts on One Target*

Assume that n mass points simultaneously contact with the tumbling object O. Velocities of n mass points are represented by $\boldsymbol{v}_i$. Let $\boldsymbol{n}_i$ represent the normal direction of the contact plane, m_i represent the mass of ith contact point, and j_i represent the magnitude of the impulse of ith contact. Therefore, the velocity of ith mass point after contact is

$$\boldsymbol{v}_i^+ = \boldsymbol{v}_i^- + j_i\boldsymbol{n}_i/m_i. \tag{6}$$

The linear and angular velocity of the target after contact are

$$\begin{aligned} \boldsymbol{v}_O^+ &= \boldsymbol{v}_O^- - (j_1\boldsymbol{n}_1 + j_2\boldsymbol{n}_2 + \cdots + j_n\boldsymbol{n}_n)/m_O \\ \boldsymbol{\omega}_O^+ &= \boldsymbol{\omega}_O^- - \boldsymbol{I}_O^{-1}(\boldsymbol{r}_1 \times j_1\boldsymbol{n}_1 + \boldsymbol{r}_2 \times j_2\boldsymbol{n}_2 + \cdots + \boldsymbol{r}_n \times j_n\boldsymbol{n}_n). \end{aligned} \tag{7}$$

In the above equation, the array of contact impulse $\boldsymbol{j}$ is undetermined,

$$\boldsymbol{j} = [j_1, j_2, \cdots, j_n]^{\mathrm{T}}. \tag{8}$$

To simplify the expression, we define the matrix of normal vectors $\boldsymbol{N}$ as

$$\boldsymbol{N} = [\boldsymbol{n}_1, \boldsymbol{n}_2, \cdots, \boldsymbol{n}_n]^{\mathrm{T}}, \tag{9}$$

and $\boldsymbol{\Sigma_{rn}}$ is defined as the following expression,

$$\boldsymbol{\Sigma_{rn}} = \sum_{i=1}^{i=n} \boldsymbol{r}_i \times j_i \boldsymbol{n}_i. \tag{10}$$

Therefore, Eq. 7 is simplified as

$$\begin{aligned} \boldsymbol{v}_O^+ &= \boldsymbol{v}_O^- - \boldsymbol{N}^{\mathrm{T}} \boldsymbol{j}/m_O \\ \boldsymbol{\omega}_O^+ &= \boldsymbol{\omega}_O^- - \boldsymbol{I}_O^{-1} \boldsymbol{\Sigma_{rn}}. \end{aligned} \tag{11}$$

Based on the impulse conservation law and introducing the coefficient of restitution e, relative velocities after contact in the direction normal to the contact plane can be derived as

$$-(e+1)v_{ri}^- = \boldsymbol{n}_i[j_i \boldsymbol{n}_i/m_i + \boldsymbol{N}^{\mathrm{T}} \boldsymbol{j}/m_O + (\boldsymbol{I}_O^{-1} \boldsymbol{\Sigma_{rn}}) \times \boldsymbol{r}_i] \tag{12}$$

On left side, the expression can be reformulated using the vector notation $\boldsymbol{v}$,

$$\boldsymbol{v} = -(e+1)[v_{r1}^-, v_{r2}^-, \cdots, v_{rn}^-]^{\mathrm{T}}. \tag{13}$$

To further simplify the expression of Eq. 12, we define

$$\boldsymbol{IC}_{ijk} = (\boldsymbol{I}_O^{-1}(\boldsymbol{r}_i \times \boldsymbol{n}_j)) \times \boldsymbol{r}_k. \tag{14}$$

Thus, the coefficient matrix is derived from Eq. 12,

$$\boldsymbol{M} = \begin{bmatrix} \frac{1}{m_1} + \frac{1}{m_O} + \boldsymbol{n}_1 \boldsymbol{IC}_{111} & \frac{\boldsymbol{n}_1 \boldsymbol{n}_2}{m_O} + \boldsymbol{n}_1 \boldsymbol{IC}_{221} & \cdots & \frac{\boldsymbol{n}_1 \boldsymbol{n}_n}{m_O} + \boldsymbol{n}_1 \boldsymbol{IC}_{nn1} \\ \frac{\boldsymbol{n}_2 \boldsymbol{n}_1}{m_O} + \boldsymbol{n}_2 \boldsymbol{IC}_{112} & \frac{1}{m_2} + \frac{1}{m_O} + \boldsymbol{n}_2 \boldsymbol{IC}_{222} & \cdots & \frac{\boldsymbol{n}_2 \boldsymbol{n}_n}{m_O} + \boldsymbol{n}_2 \boldsymbol{IC}_{nn2} \\ \vdots & \vdots & \ddots & \vdots \\ \frac{\boldsymbol{n}_n \boldsymbol{n}_1}{m_O} + \boldsymbol{n}_n \boldsymbol{IC}_{11n} & \cdots & \cdots & \frac{1}{m_n} + \frac{1}{m_O} + \boldsymbol{n}_n \boldsymbol{IC}_{nnn} \end{bmatrix}. \tag{15}$$

Equation 12 can then be rewritten as

$$\boldsymbol{v} = \boldsymbol{M} \boldsymbol{j}. \tag{16}$$

Therefore, the magnitude of the impulse of every contact is achieved by

$$\boldsymbol{j} = \boldsymbol{M}^{-1} \boldsymbol{v}. \tag{17}$$

With a computed impulse of each contacting points $\boldsymbol{j}$, the velocities after contact can consequently be derived from Eq. 6 and 7.

IV. Verification of the Contact Dynamic Model

The modeling method introduced above allows to simulate space debris capturing using a net. However, this model has to be experimentally validated. To reduce the influence by the gravity, the experiment has to be performed in a micro-gravity environment. In this case, we use a parabolic flight. This section presents the experiment and the verification.

A. Experiment

This parabolic flight experiment was led by SKA Polska under an ESA contract and was performed on board of a Falcon-20 airplane, operated by National Research Council in Ottawa, Canada. The airplane used in the experiment is a twelve-seat, two-engine business jet with the whole cabin available for micro-gravity experiments. The cabin dimensions are 4 m, 1.5 m and 1.6 m in length, width and height, respectively [23]. Due to the geometrical constraint of the airplane, the experiment had to be downscaled to fit the cabin. The net and an Envisat mockup are downscaled by a factor of 25. The Envisat mockup is firmly connected to a rig to limit the risk of the net not hitting the target. The net was shot by a pneumatic net ejector to contact the target and embrace it. The initial position of the mass center of the net is (0, 0, 0) in the local reference frame, and the position of the mass center of the target at time $t = 0$ is set as (1.5, 0, 0). Other key parameters of the parabolic flight experiment are summarized in Table 1. Definitions of some parameters can be found in [17]. Detailed information of this parabolic flight experiment is provided in [16, 20, 23].

B. Verification

The impulse-based model is to be verified by comparing the simulation of capturing a Envisat mockup with the experimental results. The initial parameters applied in the simulation are exactly the same as the parameters used in the parabolic flight experiment. Figure 5 shows the simulation of the net capturing process using the impulse-based method.

To compare the net configurations between the simulation and the experiment, some typical nodes of the net are selected and compared. In this paper, four bullets are selected because the trajectories of these four bullets are able to describe the general configuration of the net. Figure 6 provides the comparison of four bullet trajectories between the simulation and the experiment.

Table 1 Input Parameters of Parabolic Flight Experiment

Parameter	Value
Net size A [m^2]	0.8×0.8
Mesh square $-$ [$-$]	10×10
Mesh length l_0 [m]	0.08
Cable diameter d_c [mm]	1
Edge cable diameter d_e [mm]	3
Material elastic modulus E [Pa]	4.456×10^8
Bullet mass m_b [kg]	0.03×4
Shooting velocity v [m/s]	1.8
Shooting angle θ [°]	25
Distance to the target d_t [m]	1.5

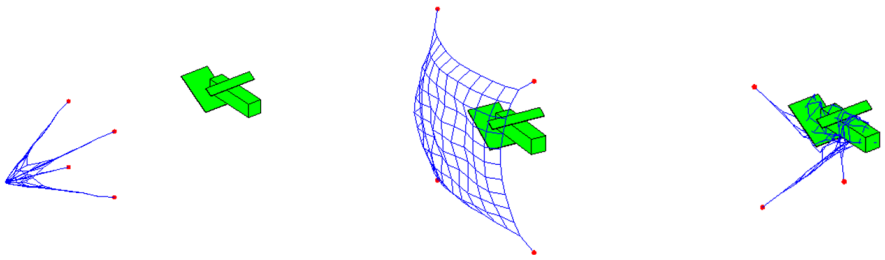

Fig. 5 Envisat mockup capturing.

However, in the simulation, the link connecting the satellite and the solar panel is not considered in the contact detection algorithm, which leads to a poor agreement of the experimental and the simulation data in the final capturing stage, such as bullet #2 in y direction and bullet #3 in z direction. Except for that, the bullet trajectories obtained from the experiment and the simulation have a good agreement with each other.

To further quantitatively analyze the difference of the simulation and the experiment, the displacement difference of these four bullet trajectories are shown using a boxplot in Fig. 7. In this figure, the diamonds in the boxes measure the average differences of the bullets trajectories. The lines in the boxes indicate the medians of each group of data. Higher whiskers represent the maximum values of the differece, and the lower whiskers represent the minimum. The sign '+' indicates

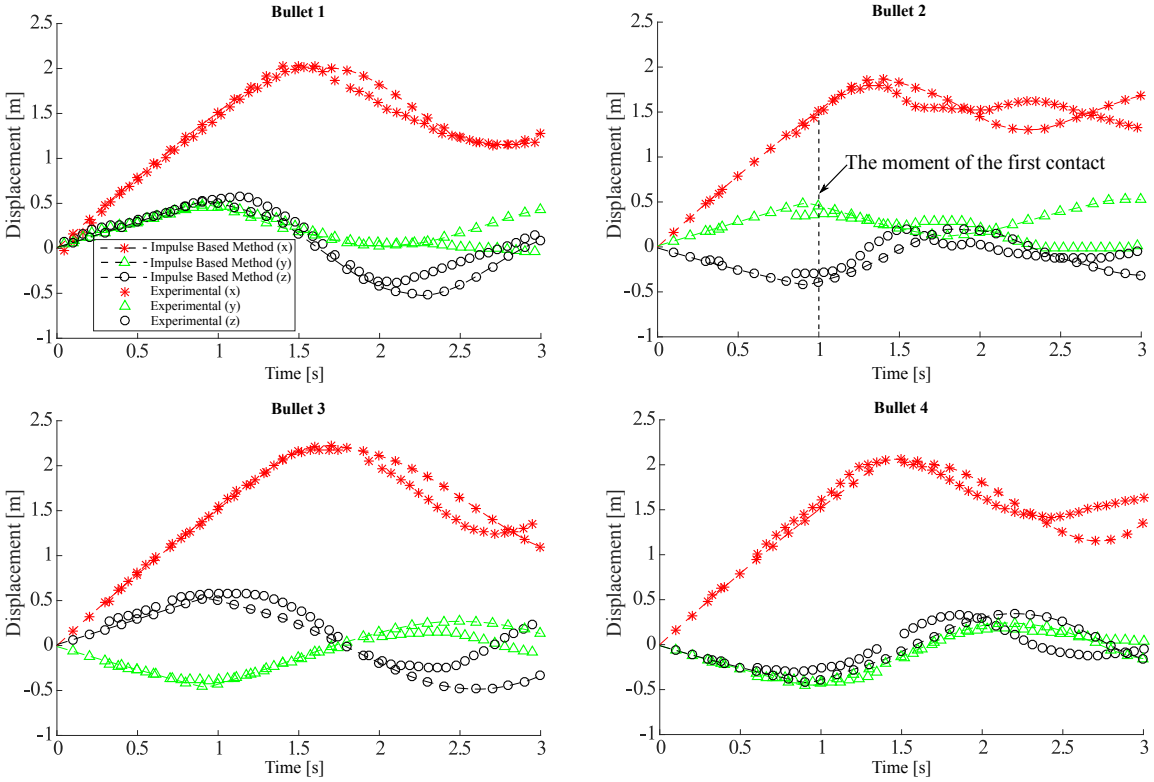

Fig. 6 Bullets trajectories under simulation and experiment.

an outlier. The largest difference arises from the bullet #3 along the z direction as explained previously. It is found that the average differences with the experiment in three directions are only 7.5 cm, 7.6 cm and 12 cm, respectively, and the average value of these differences is 9 cm.

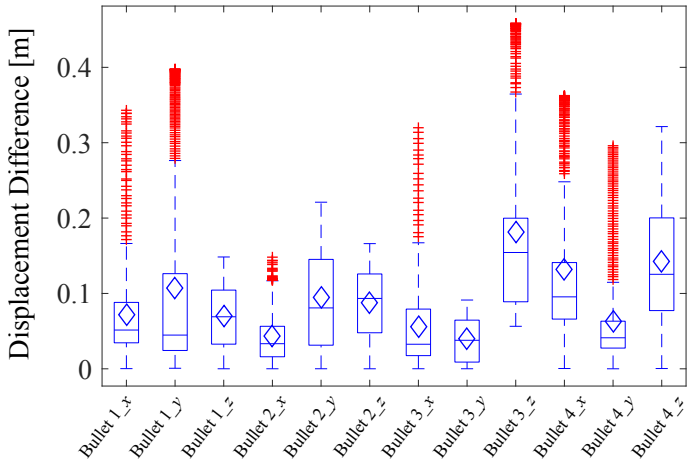

Fig. 7 Difference of bullets trajectories between simulation and experiment.

V. Tumbling Target Capturing

In the previous section, the effectiveness of the impulse-based method has been demonstrated by the parabolic flight experiment. This experiment resulted in the net becoming entangled with the Envisat mockup so that it could not be removed without cutting it, which demonstrates the effectiveness of net capturing. Therefore, a successful capturing in the simulation is defined as that if the net is able to close and embrace the target. In this section, impulse-based method is applied to investigate the capturing of a tumbling target. Here, two tumbling targets are provided as case studies: one is a three-unit cubesat, the other one is the upper-stage of rocket Zenit II. Table 2 provides the dimensions of the targets and the other simulation parameters.

Table 2 Parameters of Tumbling Targets Capturing

Parameters	Cubesat Capturing	Rocket Upper-Stage Capturing
Dimensions of the target $-$ [m]	0.1×0.1×0.3	3.9×11.047
Net size A [m^2]	0.7×0.7	30×30
Mesh square $-$ [$-$]	10×10	20×20
Mesh length l_0 [m]	0.07	1.5
Bullet mass m_b [kg]	0.03×4	1×4
Shooting velocity v [m/s]	1.8	10
Shooting angle θ [deg]	25	25
Distance to the target d_t [m]	1.4	35
Initial tumbling rate ω [rad/s]	1.5	0.5
Mass of the target m_t [kg]	3.5	8226
Mass of the net m_n [kg]	0.043	1.425
Simulation time t [s]	3	10
Integrator	Runge Kutta 4	Runge Kutta 4
Step size	$5e^{-5}$	$1e^{-4}$

A. Cubesat Capturing

Figure 8 (a) shows the reference frames of the cubesat capturing system: the inertial frame $O-XYZ$ and the body frame $o-xyz$. Its initial relative position to the net is (1.4 m, 0, 0). The three-unit cubesat is tumbling with an initial angular velocity of 0, 1, 1.5 and 2 rad/s, along the x

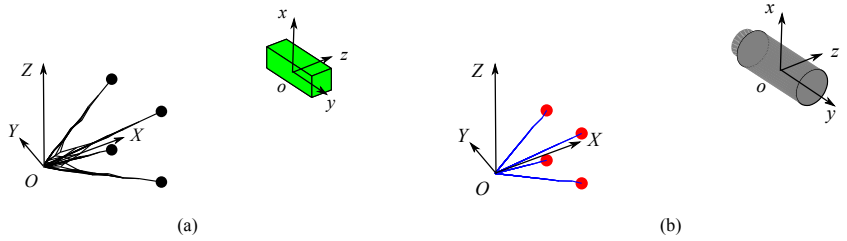

Fig. 8 Reference frames of cubesat capturing.

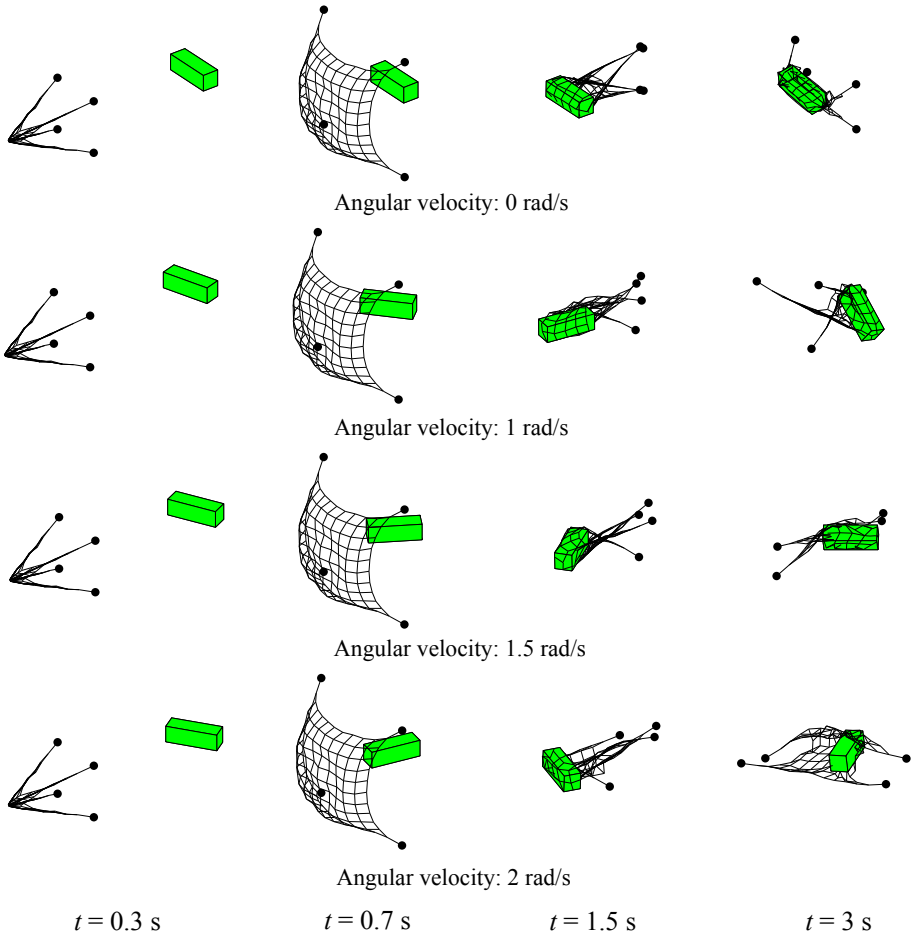

Fig. 9 Cubesat capturing under different initial tumbling rates.

direction in the body frame. Figure 9 provides the simulation process of the capture of a tumbling cubesat with different initial angular velocities. It is noticed that when the net is tumbling too fast, e.g., 2 rad/s, the net trajectory will be affected dramatically. The net is not able to close and surround the target, which leads to an unsuccessful capturing.

According to the simulations, the tumbling rate and the movement of the cubesat will be slightly affected due to the momentum exchange during the net contacting. Figure 10 shows the motion

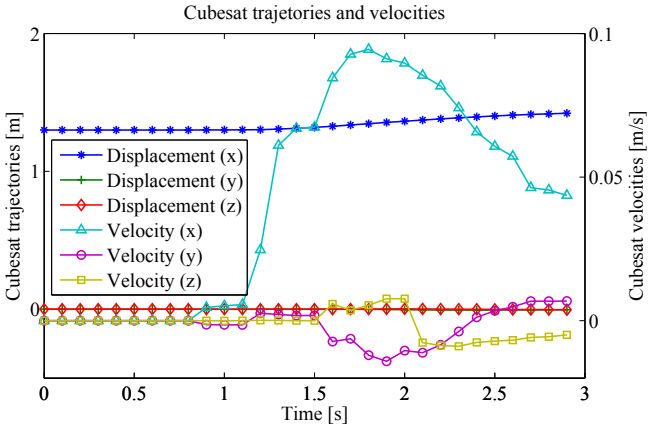

Fig. 10 Cubesat motion.

of a tumbling cubesat during capturing. As the motions of the cubesat under these four initial angular velocities are similar, only the case with 1 rad/s tumbling rate is provided. Maximum impulse during contacting is given in Fig. 11. It is found that the maximum impulse is within 3×10^{-4} Ns. Moreover, the higher the initial angular velocity, the lower the impulse at the first contact. This is because an angle is formed between the surface of the target and the velocity of the mass point. The higher the initial angular velocity, the larger the angles formed, thus the smaller the impulse exchanged. Figure 12 shows the changes of the angular velocities under different initial conditions. It is noticed that the tumbling status of a target is complex and chaotic, and the tumbling rate will be affected slightly by the net contacting. Even though the tumbling rate along its main axis is decreased slightly, it is increased along the other two axes. It also indicates that the free-throwing net itself is not able to de-tumble a target. Therefore, based on the simulations, the suggested suitable tumbling rate of a three-unit cubesat with net capturing without a dedicated closing mechanism ranges from 0 rad/s to 1.5 rad/s.

B. Rocket Upper Stage Capturing

Figure 8 (b) shows the reference frames of the rocket upper stage capturing system: the inertial frame $O-XYZ$ and the body frame $o-xyz$. Its initial relative position to the net is (35 m, 0, 0). The rocket upper stage discussed in this paper is the second stage of the rocket Zenit-II, since it is regarded as one of the most threatening space debris object to operational satellites [24].

Table 2 summarizes the parameters of the target, the net, and the initial conditions of the free-

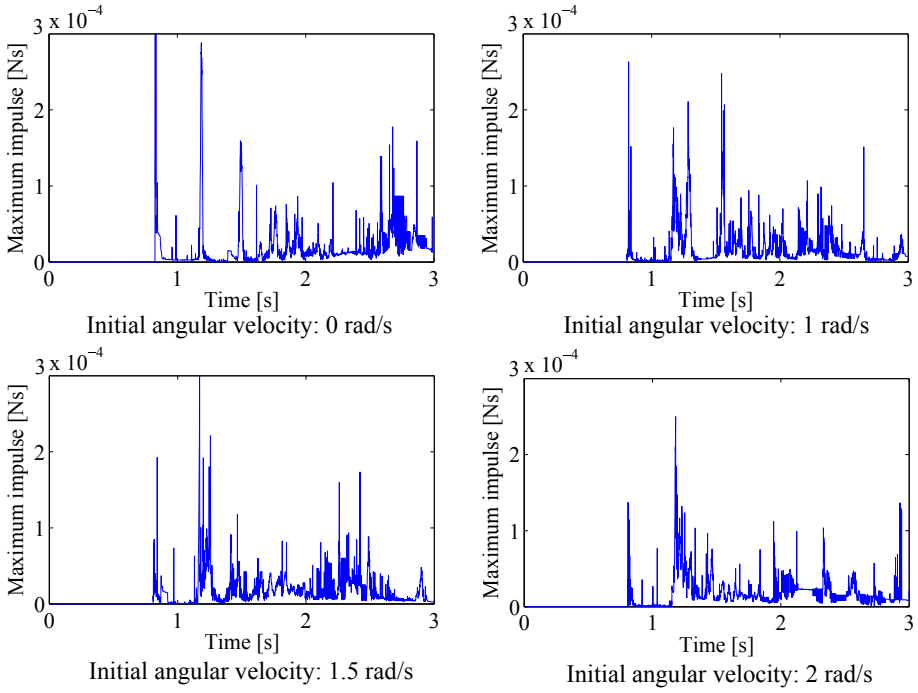

Fig. 11 Maximum impulse during contact.

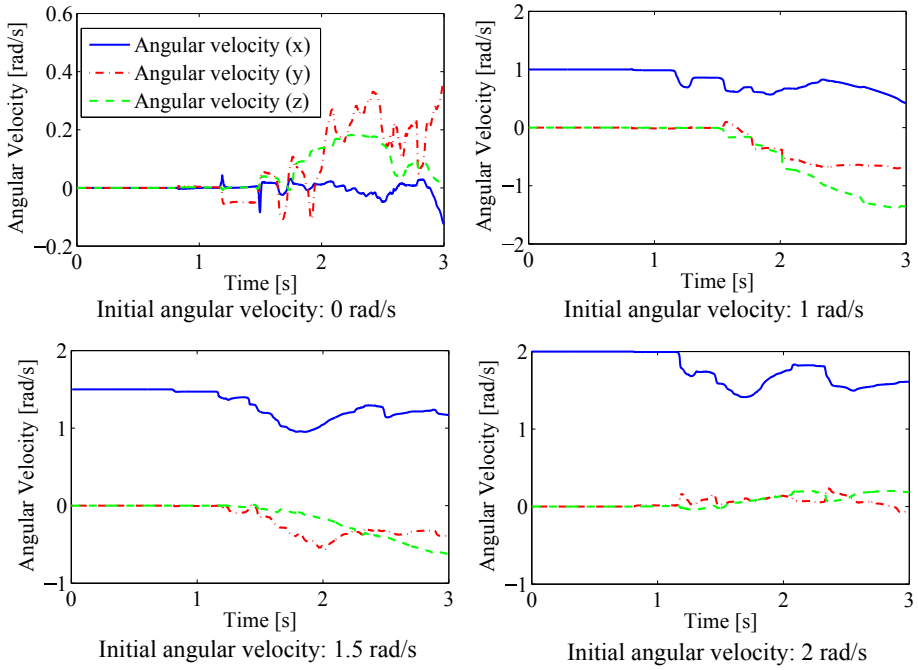

Fig. 12 Angular velocity of the cubesat during capture.

throwing deployment. The simulations of the upper stage capturing under initial angular velocity, 0.1, 0.4, 0.7 rad/s along the z axis in the body frame are presented in Fig. 13. It is found that each bullet with the connected partial net forms an arm-shaped structure, and these four arm-shaped

structures cross each other and embrace the target, such that ensuring a firm capturing. However, with the increasing initial angular velocity, the net motion will be affected more significantly, and the net tumbles together with the target. This makes the arm-shaped structures not able to cross and successfully capture the target.

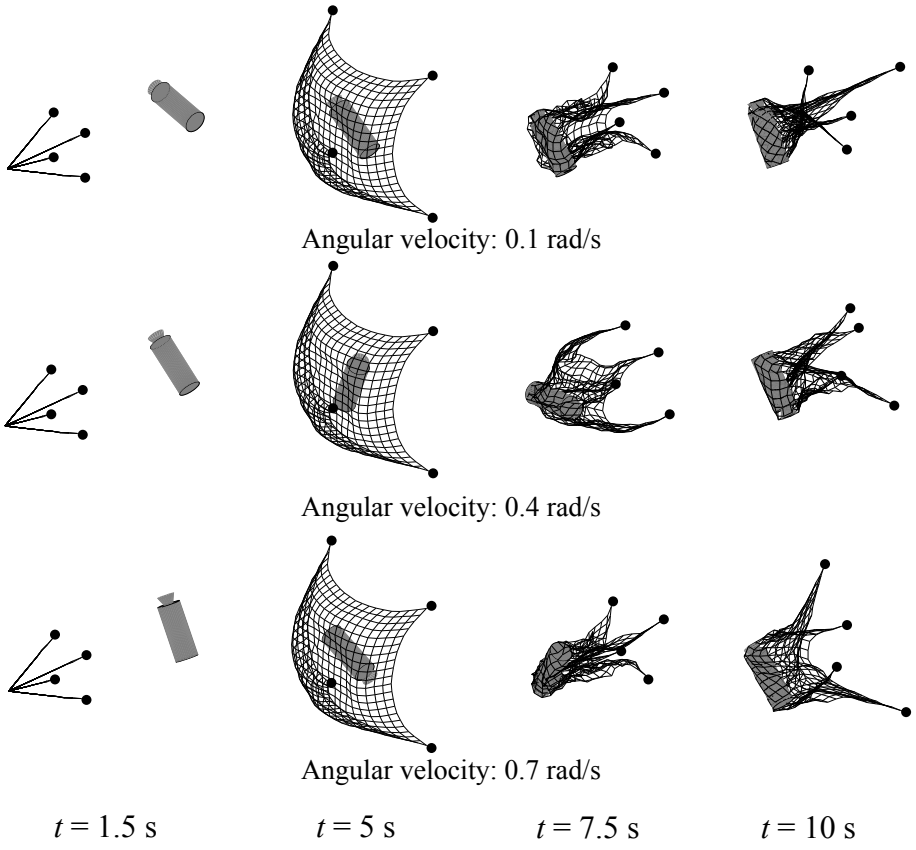

Fig. 13 Upper stage capturing (tumbling along z axis in body frame).

It becomes worse when capturing the upper stage with the tumbling axis being the x axis. The simulations of the upper stage capturing under initial angular velocities, 0.1, 0.4, 0.7 rad/s along the x axis in the body frame are presented in Fig. 14. It is noticed that the upper stage slips out of the net when its tumbling rate is as high as 0.7 rad/s. The net is able to close and surround the upper stage when the tumbling rate is smaller than that value. However, it is hard to make sure that the capturing is successful.

To overcome this weakness of the free-throwing capturing, a closing mechanism inspired by Sharf et al. [13] and Benvenuto et al. [14] is designed. The closing mechanism adopts the torsional spring mechanism installed inside the bullet as shown in Fig. 15. We utilize flexible tubes as the

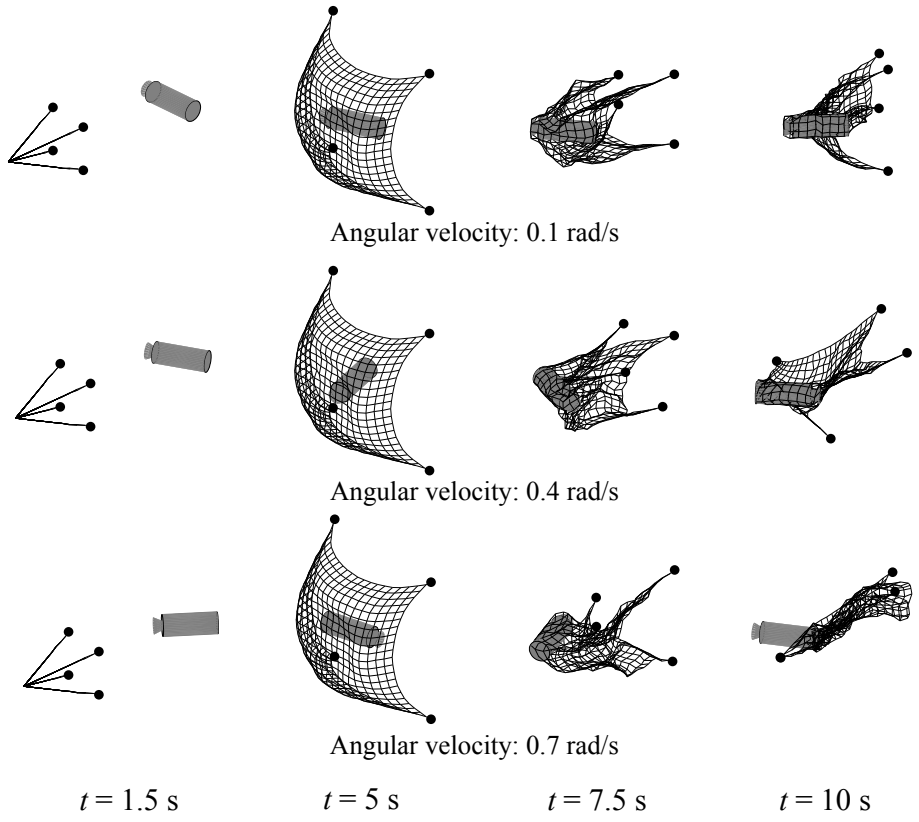

Fig. 14 Upper stage capturing (tumbling along x axis in body frame).

net perimeter and let the closing thread go through the tube then connect to the winch inside the bullets. Net cables are knotted with the outside part of the tube as well as the bullets. The closing mechanism will be trigged after the net contacts with the target, and the closing thread will be rewound into the devices in the bullets, such that four bullets start to move towards each other until the net closes. In this way, it ensures that the target is encompassed in the net and is not able to slip out. Figure 16 shows the capturing with a closing mechanism when the tumbling rate is as high as 1.1 rad/s, which ends up with a firm and successful capture. We also showed that the capturing also succeeds when the target is tumbling around z-direction as shown in Fig. 17.

VI. Conclusions

The impulse-based method has been used as contact dynamic model in scenarios of capturing of tumbling space debris objects. The theoretical solutions of single contact and multiple contacts dynamics based on the impulse-based method have been derived. Results of the parabolic flight experiment have been used to verify the contact dynamic model. The comparison of the simulation

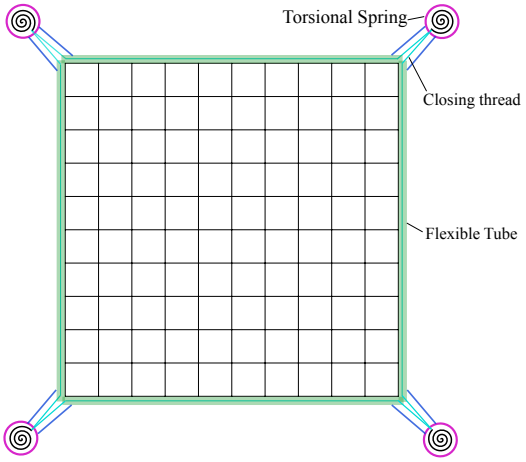

Fig. 15 Concept of a closing mechanism

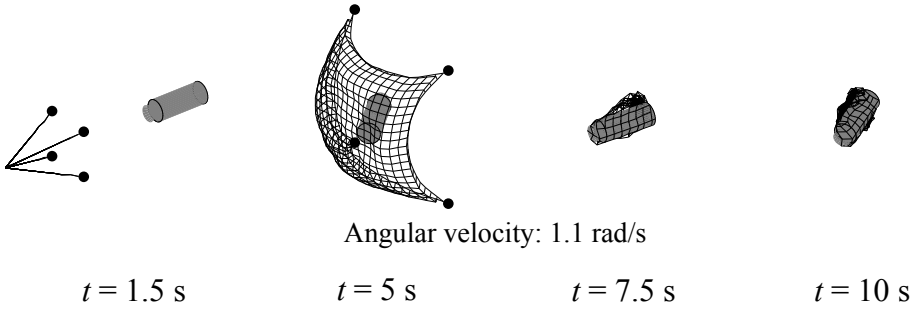

Fig. 16 Upper stage capturing with closing mechanism (tumbling along x axis in body frame).

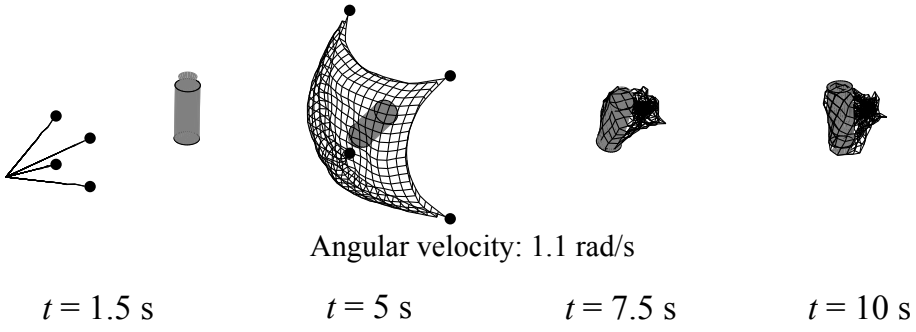

Fig. 17 Upper stage capturing with closing mechanism (tumbling along z axis in body frame).

and the parabolic flight experiment shows that the average differences in three directions are only 7.5 cm, 7.6 cm and 12 cm, respectively. Two case studies have been investigated based on the verified contact dynamic model: one is the capturing of the tumbling three-unit cubesat, and the other one is the capturing of an upper stage of rocket Zenit-II. Simulation results indicate that, for the three-unit cubesat, with a specific net configuration, it can be successfully captured when the

tumbling rate is smaller than 1.5 rad/s. However, for the rocket upper-stage, with a specific net configuration, it can be successfully captured only when the tumbling rate is smaller than 0.7 rad/s. The proposed closing mechanism is able to ensure the capturing even when the tumbling rate is beyond that threshold.

In this paper, the contact detection is not performed along cables of the net in the simulation. The discussion on the influence by this contact detection on the capturing is expected in the future.

Acknowledgments

The first author acknowledges the financial support from the Chinese Scholarship Council. The authors wish to acknowledge the assistance given by Mr. Kjetil Wormnes, Mr. Wojciech Gołębiowski and Dr. Arend Schwab. In addition, the authors would also like to acknowledge the experimental dataset shared by ESA.

References

[1] J.-C. Liou, "An active debris removal parametric study for LEO environment remediation," *Advances in Space Research*, vol. 47, no. 11, pp. 1865–1876, 2011. doi: https://doi.org/10.1016/j.asr.2011.02.003.

[2] M. Shan, J. Guo, and E. Gill, "Review and comparison of active space debris capturing and removal methods," *Progress in Aerospace Sciences*, vol. 80, pp. 18–32, 2016. doi: 10.1016/j.paerosci.2015.11.001.

[3] D. Reintsema, J. Thaeter, A. Rathke, W. Naumann, P. Rank, and J. Sommer, "DEOS–the german robotics approach to secure and de-orbit malfunctioned satellites from low earth orbits," in *Proceedings of the i-SAIRAS, Sapporo, Japan*, pp. 244–251, (2010).

[4] P. Huang, M. Wang, Z. Meng, F. Zhang, and Z. Liu, "Attitude takeover control for post-capture of target spacecraft using space robot," *Aerospace Science and Technology*, vol. 51, pp. 171–180, 2016. doi: https://doi.org/10.1016/j.ast.2016.02.006.

[5] P. Huang, D. Wang, Z. Meng, F. Zhang, and J. Guo, "Adaptive postcapture backstepping control for tumbling tethered space robot–target combination," *Journal of Guidance, Control, and Dynamics*, vol. 39, no. 1, pp. 150–156, 2016. doi: https://doi.org/10.2514/1.G001309.

[6] P. Huang, Z. Hu, and F. Zhang, "Dynamic modelling and coordinated controller designing for the manoeuvrable tether-net space robot system," *Multibody System Dynamics*, vol. 36, no. 2, pp. 115–141, 2016. doi: https://doi.org/10.1007/s1104.

[7] J. Reed, J. Busquets, and C. White, "Grappling system for capturing heavy space debris," in *2nd European Workshop on Active Debris Removal,Paris, France*, CNES, (2012).

[8] B. Bischof, L. Kerstein, J. Starke, H. Guenther, and W. Foth, "ROGER- robotic geostationary orbit restorer," *Science and Technology Series*, vol. 109, pp. 183–193, 2004.

[9] C. Billot, S. Ferraris, R. Rembala, F. Cacciatore, A. Tomassini, and R. Biesbroek, "e.Deorbit: Feasibility study for an active debris removal," in *3rd European Workshop on Space Debris Modeling and Remediation, Paris, France*, CNES, (2014).

[10] L. Yang, Q. Zhang, M. Zhen, and H. Liu, *Dynamics and Design of Space Nets for Orbital Capture*. Springer, pp.35–105, 2017.

[11] E. M. Botta, I. Sharf, A. K. Misra, and M. Teichmann, "On the simulation of tether-nets for space debris capture with vortex dynamics," *Acta Astronautica*, vol. 123, pp. 91–102, 2016. doi: https://doi.org/10.1016/j.actaastro.2016.02.012.

[12] E. M. Botta, I. Sharf, and A. K. Misra, "Contact dynamics modeling and simulation of tether nets for space-debris capture," *Journal of Guidance, Control, and Dynamics*, vol. 40, no. 1, pp. 110–123, 2017. doi: https://doi.org/10.2514/1.G000677.

[13] I. Sharf, B. Thomsen, E. M. Botta, and A. K. Misra, "Experiments and simulation of a net closing mechanism for tether-net capture of space debris," *Acta Astronautica*, vol. 139, pp. 332–343, 2017. doi: https://doi.org/10.1016/j.actaastro.2017.07.026.

[14] R. Benvenuto, S. Salvi, and M. Lavagna, "Dynamics analysis and GNC design of flexible systems for space debris active removal," *Acta Astronautica*, vol. 110, pp. 247–265, 2015. doi: https://doi.org/10.1016/j.actaastro.2015.01.014.

[15] R. Benvenuto, M. Lavagna, and S. Salvi, "Multibody dynamics driving GNC and system design in tethered nets for active debris removal," *Advances in Space Research*, vol. 58, no. 1, pp. 45–63, 2016. doi: https://doi.org/10.1016/j.asr.2016.04.015.

[16] W. Gołębiowski, R. Michalczyk, M. Dyrek, U. Battista, and K. Wormnes, "Validated simulator for space debris removal with nets and other flexible tethers applications," in *66th International Astronautical Congress, Jerusalem, Israel*, IAC, (2015).

[17] M. Shan, J. Guo, and E. Gill, "Deployment dynamics of tethered-net for space debris removal," *Acta Astronautica*, vol. 132, p. 293–302, 2017. doi: https://doi.org/10.1016/j.actaastro.2017.01.001.

[18] A. Medina, L. Cercós, R. M. Stefanescu, R. Benvenuto, V. Pesce, M. Marcon, M. Lavagna, I. González, N. R. López, and K. Wormnes, "Validation results of satellite mock-up capturing experiment using nets," *Acta Astronautica*, vol. 134, pp. 314–332, 2017. doi: https://doi.org/10.1016/j.actaastro.2017.02.019.

[19] W. Gołębiowski, R. Michalczyk, M. Dyrek, U. Battista, and K. Wormnes, "Validated simulator for space debris removal with nets and other flexible tethers applications," *Acta Astronautica*, vol. 129, pp. 229–240, 2016. doi: https://doi.org/10.1016/j.actaastro.2016.08.037.

[20] M. Shan, J. Guo, E. Gill, and W. Gołębiowski, "Validation of space net deployment modeling methods using parabolic flight experiment," *Journal of Guidance, Control, and Dynamics*, 2017. doi: https://doi.org/10.2514/1.G002761.

[21] P. Jiménez, F. Thomas, and C. Torras, "3D collision detection: a survey," *Computers & Graphics*, vol. 25, no. 2, pp. 269–285, 2001. doi: https://doi.org/10.1016/S0097-8493(00)00130-8.

[22] B. V. Mirtich, *Impulse-based dynamic simulation of rigid body systems*. PhD thesis, University of California at Berkeley, 1996.

[23] W. Gołębiowski, M. Dyrek, U. Battista, and K. Wormnes, "Validation of flexible bodies dynamics simulator in parabolic flight," in *66th International Astronautical Congress, Jerusalem, Israel*, IAC, (2015).

[24] N. van der Pas, J. Lousada, C. Terhes, M. Bernabeu, and W. Bauer, "Analysis of mission design and target selection for space debris removal by DLR's advanced study group," in *64th International Astronautical Congress, Beijing, China*, IAC, (2013).